Materials Science & Engineering A 803 (2021) 140456

Contents lists available at ScienceDirect

Materials Science & Engineering A

journal homepage: http://www.elsevier.com/locate/msea

Fracture behavior of novel biomedical Ti-based high entropy alloys under impact loading

S. Gurel [a], M.B. Yagci [b], D. Canadinc [a,*], G. Gerstein [c], B. Bal [d], H.J. Maier [c]

[a] Koç University, Advanced Materials Group (AMG), Department of Mechanical Engineering, Istanbul, 34450, Turkey
[b] Koç University Surface Science and Technology Center (KUYTAM), Koç University, Rumelifeneri Yolu, Sariyer, 34450, Istanbul, Turkey
[c] Leibniz Universität Hannover, Institut für Werkstoffkunde (Materials Science), An der Universität 2, 30823, Garbsen, Germany
[d] Abdullah Gül University, Department of Mechanical Engineering, 38080, Kayseri, Turkey

ARTICLE INFO

Keywords:
High entropy alloy
Fracture
Impact response
TiTaHfNbZr
TiTaHfMoZr
TiTaHfNb

ABSTRACT

This paper focuses on the mechanical properties and fracture behavior of newly developed body-centered-cubic-structured TiTaHfNb, TiTaHfNbZr and TiTaHfMoZr high entropy alloys (HEAs) under impact loading as part of an effort to evaluate their potential utility as implant materials. The experimental findings showed all three Ti-based HEAs have lower Young's modulus as compared to the conventionally used implant materials. Fractography analysis revealed that the TiTaHfNb HEA demonstrated significant ductility with the highest energy absorption capacity, while the TiTaHfNbZr and the TiTaHfMoZr alloys exhibited mixed mode fracture with relatively low ductility. Specifically, the reduction of ductility and energy absorption capacity under impact loading was attributed to the addition of Zr and Mo into Ti-based HEA system, which facilitates formation of additional dislocations in the microstructure due to increased lattice distortion. The current findings demonstrate that, from a mechanical point of view, the TiTaHfNb HEA could be considered as an alternative implant material for applications demanding high wear and corrosion resistance, such as hip or knee implants, and thus, warrant further investigation of the biomedical performance of this alloy.

1. Introduction

Metallic materials are extensively used in biomedical applications to support failed tissue in orthodontic and orthopaedic applications owing to their superior mechanical properties [1–4]. As compared to other biomedical metallic materials, such as stainless steel and Co-based alloys, Ti-based alloys have attracted considerable attention owing to their excellent biocompatibility combined with high strength, good corrosion and wear resistance, and relatively lower elastic moduli [2,5–7]. Specifically, the Ti–6Al–4V alloy is widely used as a common Ti-based biomedical material. However, concerns on toxicity and mechanical biocompatibility surrounding this alloy have led to the search for alternative materials [8–10]. In particular, Ti–6Al–4V contains V and Al that can damage the nervous system if released into the blood stream in long-term applications, and elastic modulus mismatch between the bone and the Ti–6Al–4V implant can lead to tissue loss, implant loosening or prostheses failure [3,5,11–17]. Therefore, nontoxic alloys with low elastic moduli have been developed to obtain enhanced biocompatibility, including Ti–6Al–7Nb, Ti–15Mo–3Nb, Ti–13Nb–13Zr, Ti–15Sn–4Nb–2Ta-0.2Pd, Ti–16Nb–10Hf, and Ti–Nb–Ta–Zr (TNTZ) system alloys, such as Ti–35.3Nb–5.1Ta–7.1Zr and Ti–29Nb–13Ta–4.6Zr [10,18–24]. Among these alloys, the TNTZ alloys stand out since all their constituent elements individually exhibit biocompatibility, and the alloys possess lower elastic moduli as compared to the Ti–6Al–4V alloy, resulting in improved fatigue and fracture characteristics in biomedical applications [25–27].

Fracture is an important consideration for implant materials, and it is strongly influenced by the microstructure [28–30]. The main concerns regarding the fracture of the implants revolve around the defects in the design and manufacturing processes, non-passive fit of the superstructure leading to unstable forces within implant-bone interfaces, and biomechanical and physiological loading factors [28,29,31]. Despite definitely having an influence, material defects such as porosity are not the main causes of fracture, yet the loading usually dictates the fracture response quite significantly [28,29,32]. Therefore, a non-passive fit may create an extra stress on an implant and bone, facilitating implant fracture [29,33]. Moreover, an adequate prosthesis design is a requirement to eliminate undesirable forces, and obtain effective durability

* Corresponding author.
E-mail address: dcanadinc@ku.edu.tr (D. Canadinc).

https://doi.org/10.1016/j.msea.2020.140456
Received 10 July 2020; Received in revised form 22 October 2020; Accepted 24 October 2020
Available online 28 October 2020

under irregular loading [28,29]. Thus, an implantable material ideally must be ductile, easy to be formed according to the desired design of an implant, and at the same time, rigid enough to withstand the applied loading. In essence, implant materials have to satisfy a large set of specific requirements, such as high corrosion resistance, high toughness and fracture resistance, in order to withstand possible degradation in aggressive environments and irregular loading that might be inevitable due to specific movements of the human body [4,6,7].

While numerous studies have been carried to develop conventional biomedical alloys with certain microstructures to satisfy the aforementioned demands, a new class of metallic materials, namely the high entropy alloys (HEAs), have recently come into focus [34,35], some of which also constitute ideal candidates for utility in biomedical applications. The HEAs can have exceptional mechanical properties such as high strength and toughness [36–46], excellent corrosion resistance [46–48], high fracture toughness [49,50] and high thermal stability [38, 46,51] brought about by their multi-principal elements leading to a high configurational entropy and thereby forming a single stable solid phase [37,47,52]. Indeed, certain HEAs exhibit good biocompatibility owing to their high corrosion resistance and protective oxide layer formation on the surface in aggressive environments [53–59].

In an effort to enhance the mechanical compatibility with the bone tissue, several HEAs with body centered cubic (BCC) structures have been developed containing early transition elements, such as Ti, Hf, Nb, Zr, Mo and Ta, in order to obtain high strength and ductility, low elastic modulus, improved fracture resistance and hardness, and thereby eliminate problems due to the loss of bone integrity that can cause sudden failure of an implant, and mechanical insufficiencies during service life [29,30,60–62]. The newly developed HEAs that consist of the early transition elements such as TiNbTaZrMo [26,61,63] showed excellent biocompatibility as compared to pure Ti and the Ti–6Al–4V alloy, and superior mechanical properties such as high strength and high workability have been obtained in HEAs such as TaNbHfZrTi that contain transition elements [43,59–61,64–68]. Moreover, some studies on HfNbTaTiZr, HfMoTaTiZr and HfMoNbTaTiZr systems revealed their high strength and ductility with relatively low elastic moduli [60,69, 70]. These alloys also seem promising due to their non-toxic constituents.

Considering the previous promising results reported on HEAs based on early transition elements, three derivatives of TiTaHf-based HEAs, namely TiTaHfNb, TiTaHfNb and TiTaHfMoZr, which contain only non-toxic transition elements, were developed in the present study. Despite the fact that a few previous studies evaluated Ti-based HEAs [59,63–66, 69–71], there is a lack of information about their fracture mechanisms in the case of a sudden failure, such as under impact loading, which is very much relevant to their utility as implants. In order to fill this gap and help evaluating the potential of these selected Ti-based HEAs as implant materials from a mechanics point of view, the focus was placed on the mechanical properties and qualitative evaluations of fracture response of the bcc-structured TiTaHfNb, TiTaHfNbZr, and TiTaHfMoZr HEAs at 298 K under impact loading. With this purpose, TiTaHfNb, TiTaHfNbZr and TiTaHfMoZr HEA samples were subjected to Charpy impact and nano-indentation tests, and thorough pre- and post-mortem microstructure analyses were performed utilizing X-ray diffraction (XRD) and scanning electron microscopy (SEM). The findings presented in this paper show that TiTaHfNb, TiTaHfNbZr, and TiTaHfMoZr HEAs have good mechanical properties and significant fracture resistance. Specifically, the TiTaHfNb alloy exhibited superior fracture toughness, and addition of Zr and Mo decreased the energy absorption capacity of the Ti-based HEA system. In addition, while the TiTaHfNb exhibited mostly ductile behavior, the TiTaHfNbZr HEA exhibited brittle and ductile regions evidencing a mixed fracture mode. Overall, the current findings indicate that these three Ti-based HEAs exhibit promising mechanical response for utility in implant applications, warranting further elaboration on their mechanical and biocompatible response.

2. Experimental procedures

In the present study, HEAs with a purity of 99.9% were produced by arc melting: the TiTaHfNb HEA was composed of 50 wt% Ti, 16.67 wt% Ta, 16.67 wt% Hf and 16.67 wt% Nb, whereas the TiTaHfNbZr and the TiTaHfMoZr compositions were equimolar. The disc-shaped multi-component alloys with a diameter of 50.1 mm and a thickness of 6.1 mm were cut by an electrical discharge machine (EDM) to obtain 10 mm × 5 mm x 1 mm bulk samples, and 45 mm × 6 mm x 3 mm impact test samples with a 1 mm deep notch at the center. The orientation of the samples with respect to the initially disc-shaped casting is schematically illustrated in Fig. 1. The samples were tested in as-cast form, and no further processing was undertaken following the production of the alloys by arc melting. The three high entropy alloys were prepared by melting of pure elements in the arc furnace with argon environment, and the samples were remelted twice. It should be noted that dimensions of the V-notch specimens utilized in the impact tests were adjusted to the test equipment in accord with the Charpy impact test standards [72] (Fig. 1). Charpy impact testing, also known as the Charpy V-Notch test (CVN), was performed on the three aforementioned HEAs at 298 K utilizing a TERCO MT3016 impact tester with a 15 J capacity, followed by an analysis of fracture surface of the samples carried out on a Zeiss Ultra Plus field emission SEM (FESEM).

The surfaces of the bulk samples were mechanically ground with SiC emery papers with coarseness ranging from 106 to 2.5 μm, then polished with 0.30 μm alumina slurry. Thereafter, the bulk samples were cleaned ultrasonically with ethanol and rinsed with deionized water. Following the polishing/cleaning procedure, crystallographic characterization of the samples was carried out with a Bruker D2 Advanced X-ray diffractometer (XRD) using a Cu-Kα radiation source. The XRD was operated at 30 kV and 10 mA with an incidence angle of 5°, and the scanning region ranged from 5° to 90° with a 0.02° increment.

In order to generate the stereoscopic three-dimensional morphology of the fracture surfaces of the specimens at the micro-scale, a KEYENCE

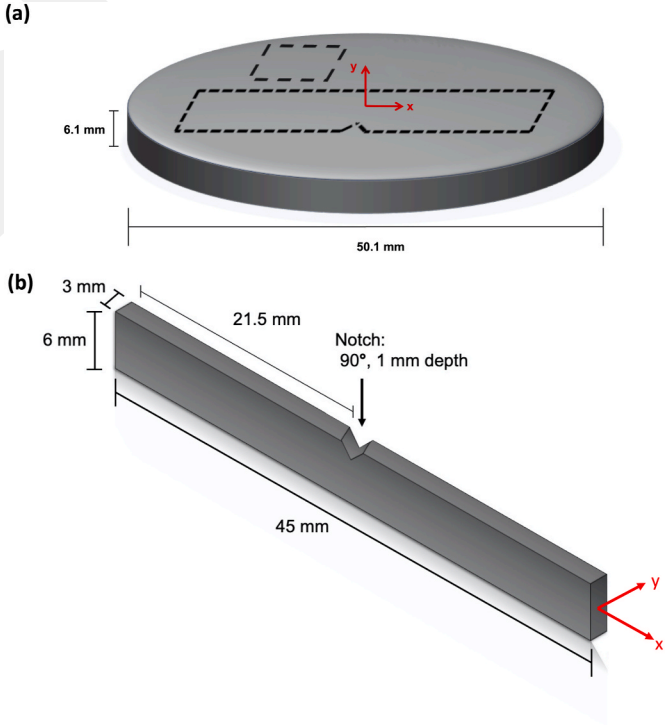

Fig. 1. **(a)** Schematic showing the dimensions of the as-cast disc-shaped alloys and the extraction orientations of the bulk (10 mm × 5 mm x 1 mm) and the V-notch specimens (45 mm × 6 mm x 3 mm), **(b)** schematic showing the dimensions of the V-notch samples.

super-depth-of-field 3D-dimensional micro system (VHX 1000E; Keyence) was used. For transmission electron microscopy (TEM), lamellae were cut directly from the centers of the deformation zones right underneath the fracture surfaces by means of focused ion beam (FIB) utilizing Ga-ions with a resolution of 2.5 nm and on a Zeiss AURIGA FE-SEM-FIB double beam system. The TEM analyses were performed on a JEOL JEM2010 transmission electron microscope with a 200 kV electron gun.

Mechanical characterization of the bulk HEAs was accomplished by room-temperature compression experiments and nano-indentation tests. The compression experiments were carried out on a servo-hydraulic Instron universal test frame equipped with a digital extensometer; and the compression samples with dimensions of 4 mm × 4 mm x 10 mm were deformed at a medium strain rate of 5 x 10^{-4} s^{-1}. The nano-indentation experiments were carried out on Agilent G200 tester with a Berkovich type indenter in load-control mode at a maximum applied load of 300 mN. The indentation load was applied 15 times per sample to probe microstructural variation, and each indentation test was performed under a loading/unloading rate of 30 mN with a 10 s hold time at maximum load before unloading.

Non-destructive micro-scale tomography to detect internal defects of the as-cast samples was conducted on a ZEISS Xradia 520 Versa X-ray microscope (XRM). The samples were illuminated through an aperture in front of the X-ray source. Both the sample absorption and diffraction information were recorded with a high-resolution detection system. A beam stop was added to the setup to block out the direct beam and enhance the contrast of the diffraction signal. The images were obtained with a voxel size of 3.5 μm, which was suitable for the macro-scale level samples. The evaluation was performed with the Dragonfly 4.1 software.

3. Results and discussion

The initial microstructural characterization of single-phase TiTaHfNb, TiTaHfNbZr and TiTaHfMoZr HEAs was carried out by XRD, where the experimental lattice parameters and the corresponding peak values were calculated using Bragg's law (Fig. 2). The results confirmed that the TiTaHfNb, TiTaHfNbZr and TiTaHfMoZr HEAs have a bcc structure, and the lattice constants are 3.329 Å, 3.340 Å, and 3.362 Å, respectively. These three HEAs are newly developed and there is a very limited number of studies on their properties, however the peak values and the lattice parameters are consistent with the literature [43, 60,73–76].

The CVN experiments were performed in order to assess the energy absorption capacities of TiTaHfNb, TiTaHfNbZr and TiTaHfMoZr HEAs, and reveal their fracture mechanisms under a sudden load. Impact energy values are provided in Fig. 3, and it should be noted that CVN test results are reported in Joules instead of impact energy per area since the data can be affected by the specimen size as sub-sized specimens were used in this study as required by the particular Charpy impact tester utilized. As illustrated in Fig. 4, the TiTaHfNb sample exhibited significantly different behavior, such that it was not completely broken into pieces, and the test was repeated twice to ensure that the observed response was not sample specific. The average impact energy was measured as 14.8 J in the CVN tests of TiTaHfNb. On the other hand, significantly lower impact energy values were exhibited by TiTaHfNbZr and TiTaHfMoZr HEAs, namely 0.25 J and 0.1 J, respectively (Fig. 3). Following the CVN experiments, the surface morphologies of the CVN samples were analyzed in the SEM to understand the fracture mechanism of the HEAs. The corresponding SEM micrographs from the inspection area of the TiTaHfNb HEA (Fig. 5(a)) indicate evidence of ductile behavior, namely a significant tearing pattern, and a predominately cup-and-cone type of fracture surface is evident (Fig. 5(b)). On the other hand, a closer look at the tearing patterns (Fig. 5(c)) reveals flat surfaces with Chevron marks (Fig. 5(d)) and cleavage facets in relatively small areas as compared to the ductile zones (Fig. 5(e)). Consequently, both ductile and brittle fracture modes are active in the

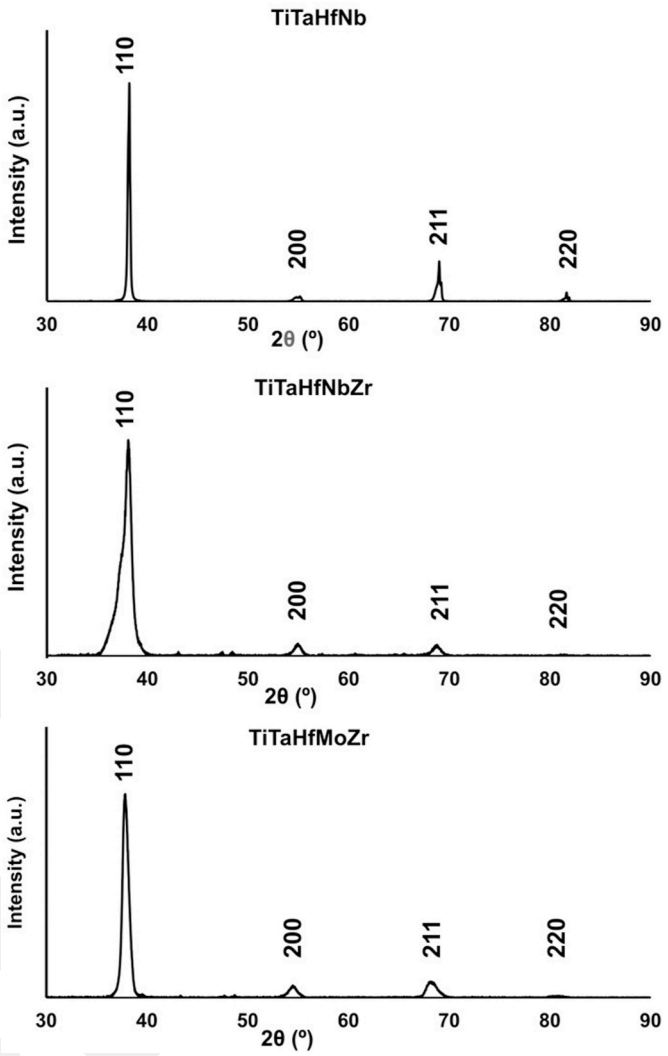

Fig. 2. XRD results showing the 2θ-scans of the as-cast **(a)** TiTaHfNb, **(b)** TiTaHfNbZr, and **(c)** TiTaHfMoZr HEAs.

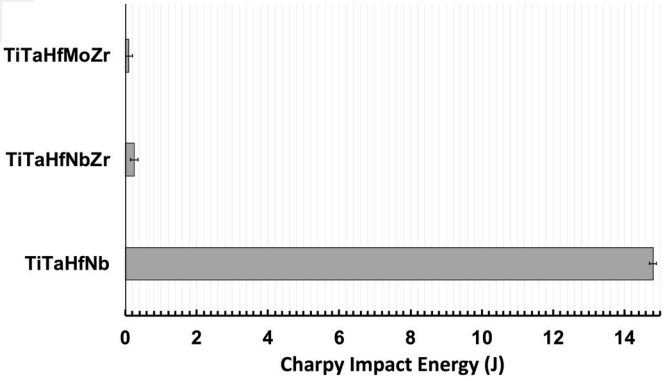

Fig. 3. Comparison of the Charpy impact energies exhibited by the TiTaHfNb, TiTaHfNbZr and TiTaHfMoZr HEAs following the CVN experiments.

TiTaHfNb HEA, as evidenced by the coexistence of cup-and-cone structures and shiny fracture zones with cleavage facets. It can be deduced that ductile mode dominates the fracture of TiTaHfNb under impact loading despite the presence of brittle regions.

In comparison to the TiTaHfNb HEA, the TiTaHfNbZr alloy exhibits a more complicated fracture surface with coexisting slant and flat regions,

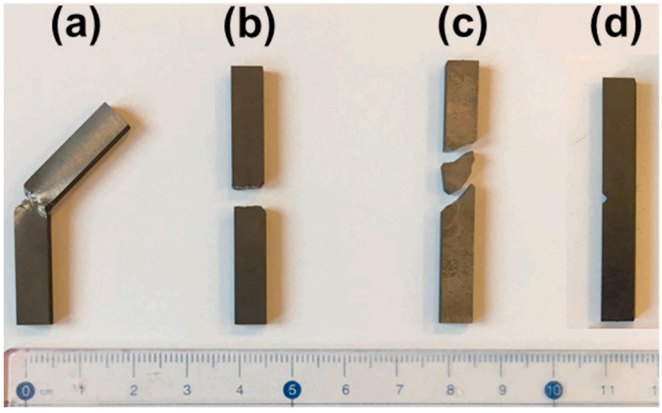

Fig. 4. The CVN test samples of **(a)** TiTaHfNb, **(b)** TiTaHfNbZr, and **(c)** TiTaHfMoZr HEAs following the experiment; **(d)** representative untested CVN test sample.

where both dull and shiny surface zones can be macroscopically seen (Fig. 7). In particular, small and shiny angular facets form in a rock-candy like morphology (Fig. 7(a)), which can be attributed to intergranular crack formations along the grain boundaries, which hints at brittle failure (Fig. 6(b) and (c)). Moreover, Chevron marks and river patterns observed on the fracture surface with cavity formations (Fig. 6 (b)) mainly result from brittle fracture: the red lines in Fig. 6(b) represent the propagation path of chevron marks that point at the crack origin, and the blue lines highlight the river lines and cleavage surfaces near the region that has elongated dimples. Moreover, cracks along grain boundaries are clearly seen in Fig. 6 with the elevation difference between the grains, such that the surface appearance indicates rapid fracture (Fig. 6(b)). Fig. 6(c) demonstrates the significant differences in the fracture patterns on TiTaHfNbZr, such that there is a transition zone formation with ladder-like structures between the smooth (left) and the non-smooth (right) regions. Indeed, a closer look at Fig. 6(d) reveals this brittle response while the river-like patterns and striations can be observed in the transition zone, and elongated dimples constitute evidence of shear forces acting on the material during fracture. Specifically, the lines on the surface of the layered structures are chevron marks, and the corresponding path is indicated by the arrows in Fig. 6(d). On this surface both ductile features with small elongated dimples and brittle ones with chevron marks and ladders can be observed. Moreover, the fracture surface of TiTaHfNbZr contains brittle and ductile zones throughout the fracture surface (Fig. 6(e)), and a closer look at these regions reveals tilt and twist formation due to misorientation between the adjacent grains [77] on the cleavage zone (Fig. 6(g)),and small dimples around the grain boundaries due to rapid cracking (Fig. 6(h)), as well as equiaxed dimples due to shear forces and ductile behavior (Fig. 6 (f)). Accordingly, despite the fact that the fracture surface of the TiTaHfNbZr HEA is dominated by cleavage, ductile regions are evident, including elongated dimples due to tearing process and shear forces. On

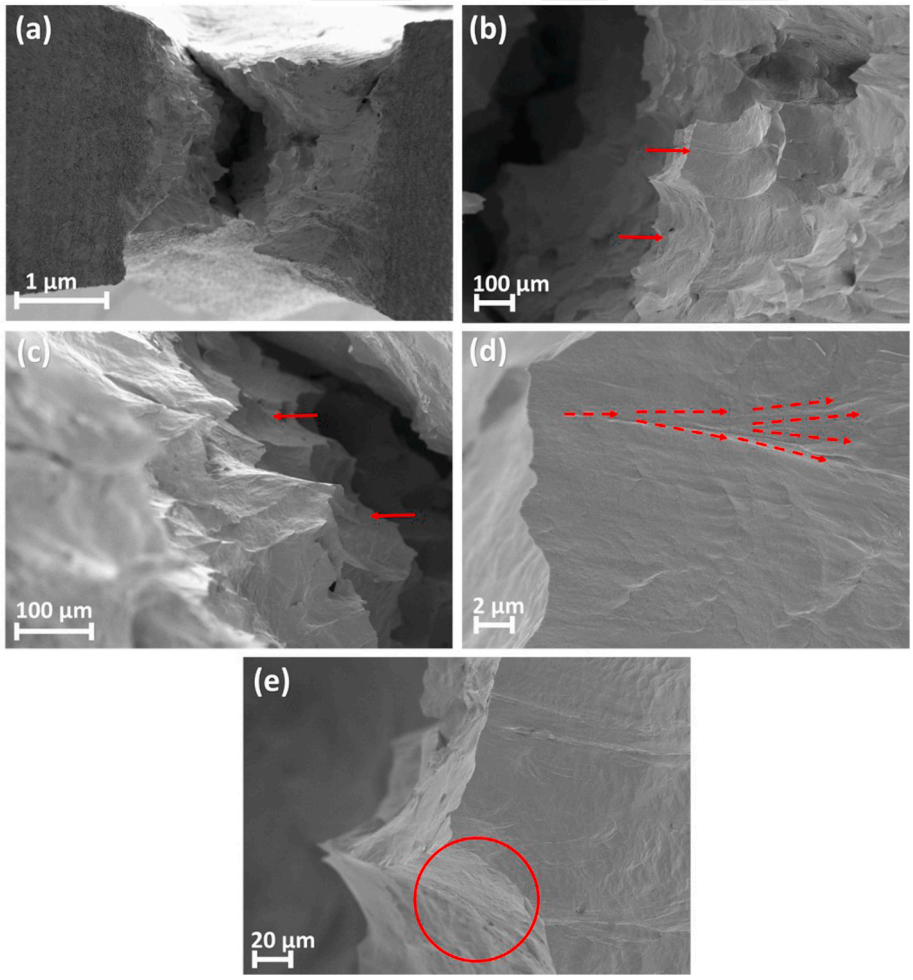

Fig. 5. SEM micrographs of TiTaHfNb HEA fracture surface: **(a)** overview, **(b)** tearing patterns, and cup-and-cone structures, **(c)** tearing region, **(d)** flat surface with Chevron marks (red lines), and **(e)** cleavage surface (red circle). (For interpretation of the references to colour in this figure legend, the reader is referred to the Web version of this article.)

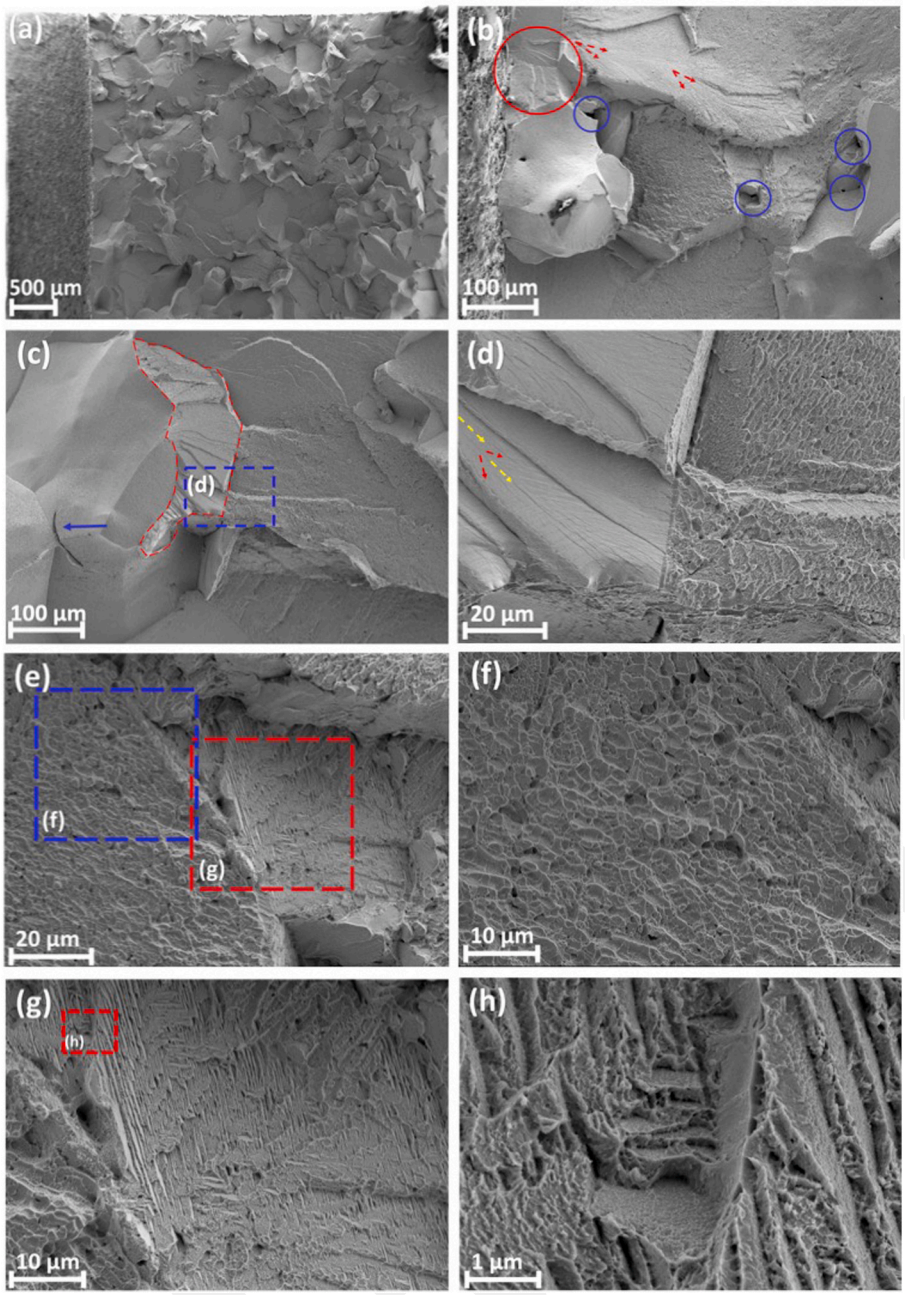

Fig. 6. SEM micrographs of the fracture surface of TiTaHfNbZr HEA: **(a)** rock-candy-like surface, **(b)** inter-crystalline structures, river patterns and ladder-like structures (red circle), where the red lines represent propagation of Chevron marks and the blue circles indicate cavity formations, **(c)** smooth and rough regions coexist where the red boundary represents the transition zone, **(d)** close-up view of the transition zone and the rough surface, with river patterns and elongated dimples, respectively, **(e)** coexisting ductile and brittle zones, **(f)** elongated dimples, **(g)** cleavage zone with twist and tilt structures, **(h)** close-up view of dimples along grain boundaries, and nano-pores. (For interpretation of the references to colour in this figure legend, the reader is referred to the Web version of this article.)

the other hand, the elongated dimples are not prevalent on areas larger than the cleavage surfaces. Thus, one can conclude that the TiTaHfNbZr HEA also exhibits a mixed fracture mode under impact loading, with the brittle mode dominating.

In the case of the TiTaHfMoZr HEA, mainly quasi-cleavage fracture features with flat facets, river patterns and Chevron marks that can be observed on the fracture surface, indicating a brittle behavior (Fig. 7). Moreover, both intercrystalline and transcrystalline fracture are facilitated with limited crack propagation (Fig. 7(a), (b) and (c)). Tongue formation, which is a result of small-scale height elevations, can also be observed (Fig. 7(b)), which can be attributed to twinning [78], where the twin boundary fracture [79] may lead to the formation of the ladder-like structures with an elevation difference as illustrated by the yellow dashed lines in Fig. 7(c). In addition, the ladder-like formations (Fig. 7(c) and (d)) due to cleavage fracture and striations that are directed gradually along shear forces (Fig. 7(e)) indicate a rapid fracture. Furthermore, flat regions with striations due to rapid fracture dominate the fracture surface of the TiTaHfMoZr HEA (Fig. 7). Therefore, cleavage fracture dominates the fracture surface of the TiTaHfMoZr HEA, and the material exhibits a much more brittle behavior than TiTaHfNb and TiTaHfNbZr with the lowest recorded impact energy of 0.1 J. These findings are also supported by the stereoscopic microscopy images presented in Fig. 8: the fracture surface of the TiTaHfNb exhibits mainly cup and cone structures, indicating ductile behavior (Fig. 8 (a) and (b)), while the flat regions and intergranular cracking with small dimples on the fracture surface of the TiTaHfNbZr HEA clearly evidence its mixed fracture mode with higher brittleness (Fig. 8 (c) and (d)). As for the TiTaHfMoZr alloy, cleavage surfaces were observed under the stereoscopic microscope, supporting the aforementioned brittle response of this alloy under impact loading (Fig. 8 (e) and (f)).

In order to compliment the impact tests, compression experiments were also carried out at room temperature (Fig. 9). The results showed that the TiTaHfNb HEA exhibits a significantly larger toughness as compared to the other two HEAs despite its lower strength, which stands

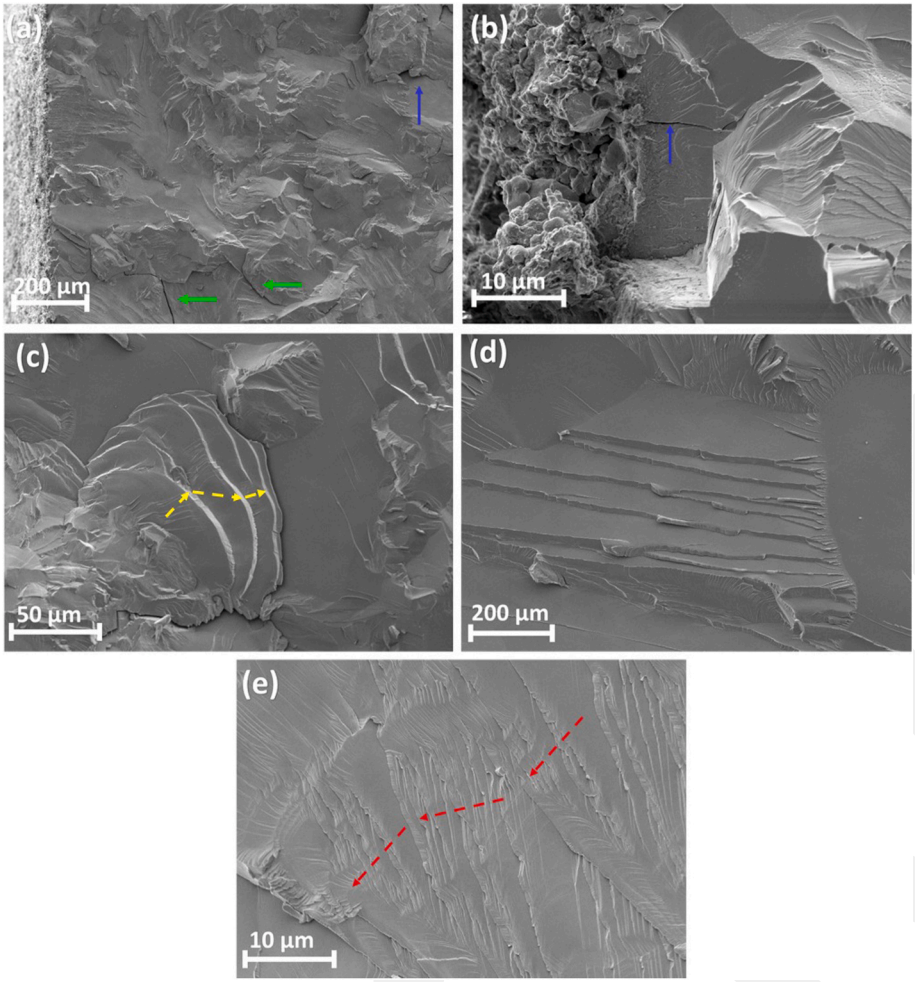

Fig. 7. SEM micrographs of fracture surface of the TiTaHfMoZr HEA: **(a)** green and blue arrows indicate intergranular and transgranular fracture, respectively, **(b)** tongues and river patterns, where the blue arrow indicates transgranular fracture, **(c)** twin boundary fracture, ladder-like structures, and intergranular fracture, **(d)** cleavage surface, and **(e)** striations directed along shear. (For interpretation of the references to colour in this figure legend, the reader is referred to the Web version of this article.)

in good agreement with the impact energy comparison provided in Fig. 3. In addition to compression experiments, the Young's moduli of TiTaHfNb, TiTaHfNbZr and TiTaHfMoZr were also measured by nano-indentation (Fig. 10), and determined as 112.2 GPa, 131.6 GPa and 158.9 GPa, respectively. Even though these values are still far from that of the bone which is about 30 GPa [11,80], they are significantly lower as compared to the commonly utilized biomaterials such as 316 L stainless steel and Co-based alloys with elastic moduli within the 180–210 GPa range [11], offering an enhancement in terms of mechanical compatibility with the bone. The nano-indentation tests also provided the hardness values for the three HEAs studied in Fig. 11, which were measured as 3.5 GPa for TiTaHfNb, 6.5 GPa for TiTaHfNbZr, and 6.6 GPa for TiTaHfMoZr. Accordingly, TiTaHfNbZr and TiTaHfMoZr are almost twice as hard as TiTaHfNb, demonstrating the effectiveness of Zr and Mo addition as a means of increasing the hardness of Ti-based HEA system, which can be attributed to solid solution strengthening [81].

Load – displacement curves obtained from the nano-indentation experiments of the three HEAs are provided in Fig. 10. Accordingly, the TiTaHfNb HEA exhibits larger ductility as compared to TiTaHfNbZr and TiTaHfMoZr when all samples were loaded up to 300 mN and then unloaded. This difference in ductility is the reason for the TiTaHfNb HEA's ability to absorb greater energy than TiTaHfNbZr and TiTaHfMoZr under impact loading. The addition of Mo and Zr to the Ti-based HEA system also changes the microstructure while dendritic structures are evident in TiTaHfMoZr as observed by EDX and BSE (Fig. 12). Moreover, although some dendrites have also been observed in the TiTaHfNbZr microstructure (Fig. 13(c)) there is no apparent difference in chemical composition between the matrix and the dendrites of this HEA as opposed to the case of TiTaHfMoZr (Figs. 12 and 13(d)). As evident from the bright-field microscopy images of TiTaHfMoZr in Fig. 13 (e)–(g), the cracks propagate through the dendrites but not within the interdentritic regions. On the other hand, TiTaHfNb has a homogenous microstructure without dendritic regions (Fig. 13 (a) and (b)), and thus it exhibits more stability against cracking (Fig. 13 (a) and (b)). Cracking mainly occurs along the grain boundaries (Fig. 13 (a) and (b)), and there is no further cracking on the fracture surface of the TiTaHfNb HEA. Indeed the TEM images of the fractured TiTaHfNb HEA samples exhibit carbides around the grain boundaries (Figs. 13(a) and 14(a)), which can facilitate cracking by enhancing brittleness around the grain boundaries. In this context it should be noted that impurities and interstitials can significantly alter an alloy's deformation response [82], especially in terms of ductility, yet the exact effect can be difficult to assess [83]. In the current materials, and specifically in the case of the TiTaHfNb HEA, the trace amount of C originates from the arc melting furnace, and found its way to some grain boundaries. Since the focus of the present study was on the assessment of the impact/fracture response of these Ti-based HEAs for the first time, a detailed elemental analysis of the microstructure is left for future work focusing on the formability of these alloys, where the impurity content and interstitials play a crucial role. Moreover, dendritic structures were also observed in TiTaHfNbZr (Fig. 13(c)), however; cracking behavior is less stable than it is in TiTaHfNb, yet more stable as compared to TiTaHfMoZr. TEM results (Fig. 14(b)) indicate that slip becomes more prevalent under impact loading within small grains upon addition of Zr to TiTaHfNb.

The CVN experiments and the corresponding microstructural

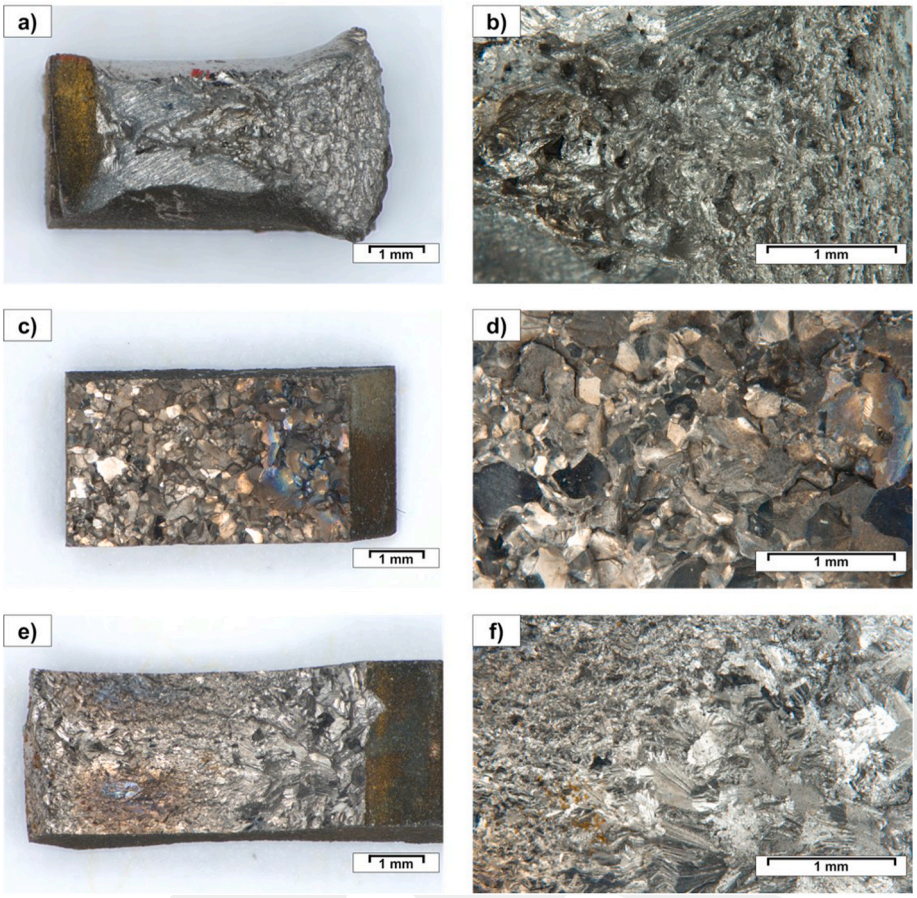

Fig. 8. Stereoscopic microscopy images of the fracture surfaces of the studied HEAs following the CVN tests: **(a)** and **(b)** TiTaHfNb, **(c)** and **(d)** TiTaHfNbZr, and **(e)** and **(f)** TiTaHfMoZr.

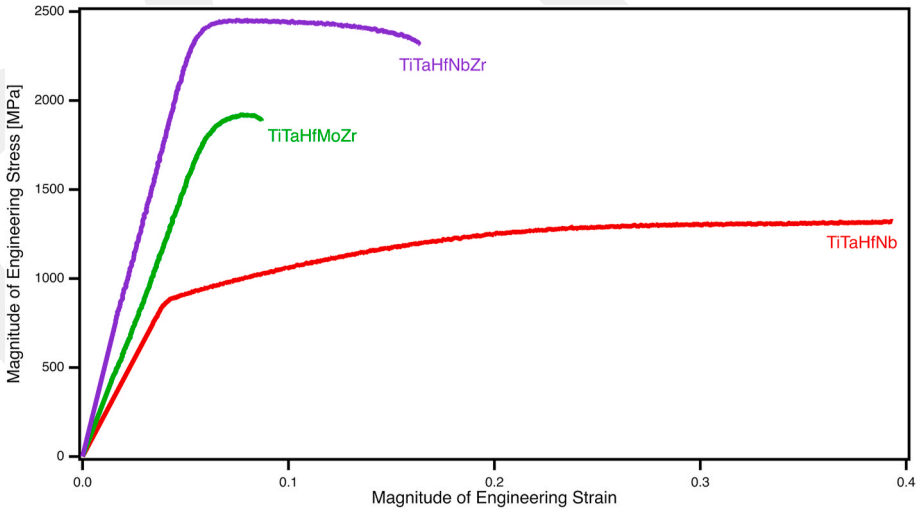

Fig. 9. Compressive deformation response of the three HEAs investigated in this study; the experiments were carried out at room temperature and a strain rate of 5 x 10^{-4} s^{-1} and each curve represents the average of three experiments carried out on companion samples.

analyses demonstrated that modifications made to the elemental compositions of Ti-based HEAs significantly influence the fracture behavior. Specifically, addition of Zr to TiTaHfNb notably decreased the impact energy and enhanced the brittleness, where the impact energy decreased from an average of 14.8 J down to 0.25 J. Yet the lowest energy absorption capacity was observed in the case of TiTaHfMoZr HEA, namely 0.1 J, and this alloy also exhibited the most brittle response. This can be attributed to the formation of multiple phases by Mo addition (Fig. 12 (a) and (b), Fig. 13 (d)–(g)) [59,61,84,85]. The corresponding EDX analyses, BSE and bright-field microscope images revealed that a non-homogenous microstructure with dendritic and interdendritic regions is present, as evidenced by Ta-rich and Zr-rich, compositions, respectively. Moreover, there are non-homogenous fracture patterns present on the fracture surface of TiTaHfNbZr: this HEA exhibits strictly

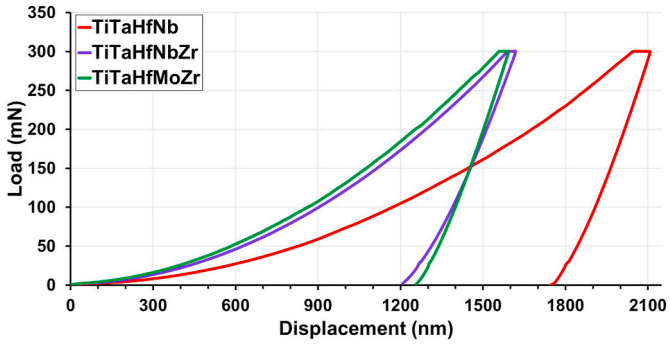

Fig. 10. Load vs displacement data for TiTaHfNb, TiTaHfNbZr, TiTaHfMoZr HEAs as obtained by nano-indentation experiments.

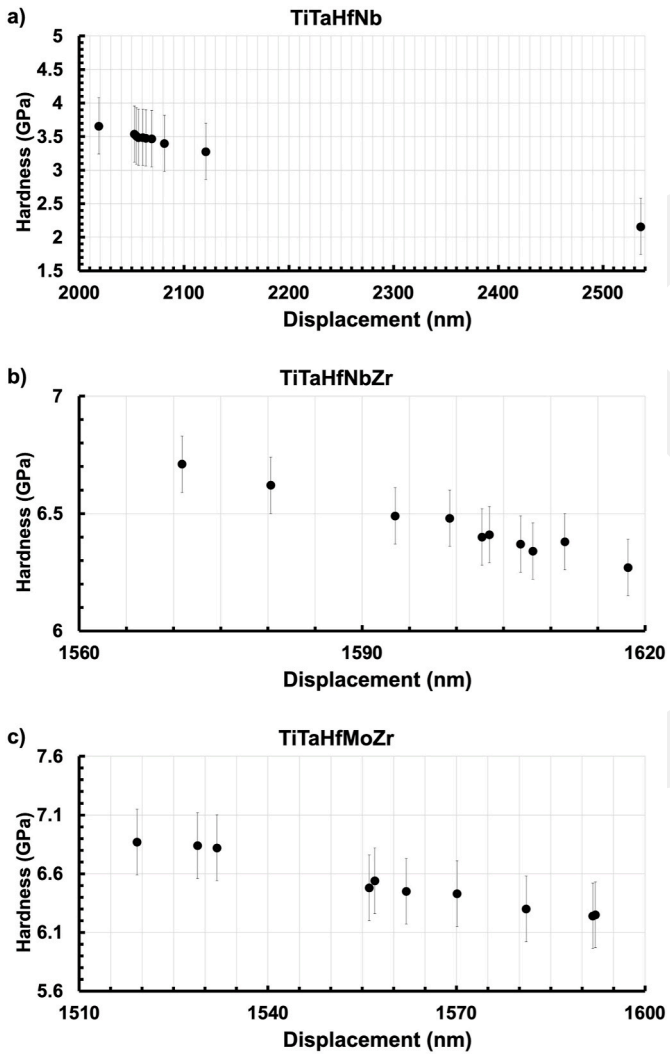

Fig. 11. Hardness vs displacement data for **(a)** TiTaHfNb, **(b)** TiTaHfNbZr, and **(c)** TiTaHfMoZr HEAs as obtained from nano-indentation experiments.

defined and coexisting fracture regions of brittle and ductile nature (Figs. 8 and 9). An EDX analysis revealed that the constituents of TiTaHfNbZr are homogenously dispersed in the microstructure (Fig. 10 (c) and (d)). While there is no crack on the fracture surface of TiTaHfNb and cracking occurs along the grain boundaries of TiTaHfNb as illustrated in Fig. 13 (a) and (b), transgranular cracking exhibits on the fracture surface of TiTaHfNbZr as can be seen in Fig. 13 (c). The difference between the fracture surface of TiTaHfNb and TiTaHfNbZr can be attributed to Zr addition in the Ti-based HEA that leads to enhanced dislocation activity. Such that, TEM results of TiTaHfNbZr reveal slipping in smaller grains of TiTaHfNbZr. Addition of Zr may lead to slipping in small grains, and therefore transgranular cracking occurs on the fracture surface of TiTaHfNbZr.

In order to probe the as-cast samples for defects, samples extracted from the bulk discs were subjected to XRM, which showed that a negligible volume fraction of interdendritic voids typical in as-cast alloys was present in the samples (Fig. 15)[1]. Other microstructural issues such as local segregation of some elements were also minimal, and the HEAs tested in their as-cast forms already exhibited superior impact response. Still, it is expected that the performance of these alloys could be further enhanced by processing, such as hot isostatic pressing or similar techniques.

Overall, the current experimental findings demonstrate that the addition of Zr and Mo into Ti-based HEA system facilitates formation of additional dislocations in the microstructure due to increased lattice distortion, as well as increased hardness, and reduces ductility and energy absorption capacity. The fracture surface micrographs of the three HEAs revealed that the TiTaHfNb alloy exhibits the most ductile behavior under impact loading, while TiTaHfNbZr and TiTaHfMoZr exhibit significantly lesser ductility. These results imply that TiTaHfNb HEA could be considered as an attractive alternative material for applications suffering from both wear and corrosion, such as hip or knee implants, and thus, warrant further investigation of the mechanical and biomedical performance of this alloy.

4. Conclusions

Fracture response of three Ti-based high-entropy alloys (HEAs), namely TiTaHfNb, TiTaHfNbZr and TiTaHfMoZr alloys, was investigated employing Charpy impact tests carried out at 298 K.

- TiTaHfNb HEA has the highest energy absorption capacity and exhibits a more ductile behavior as compared to the TiTaHfNbZr and TiTaHfMoZr HEAs.
- The presence of Zr in the substrates led to a decrease in impact energy, and the TiTaHfNbZr exhibited mixed fracture characteristics with predominantly brittle behavior.
- Mo addition resulted in an inhomogeneous microstructure (TiTaHfMoZr), leading to dendrite formation and significant decrease in energy absorption capacity; and cleavage surfaces and quasi-cleavage structures were evident upon brittle fracture of this HEA.
- Zr and Mo addition to the TiTaHfNb HEA system resulted in significantly enhanced dislocation activity in the microstructure under loading.

Overall, the findings reported herein not only demonstrate the potential of the Ti-based HEAs to be utilized as implant materials, but also warrant further investigation of their mechanical response and biocompatibility prior to their utility in medical applications.

Data availability

Both the raw and processed data required to reproduce these findings can be obtained upon request from the corresponding author.

CRediT authorship contribution statement

S. Gurel: Formal analysis, Investigation, Methodology, Validation,

[1] The XRM was carried out on all three HEAs, yet due to the similarity of the results and for the sake of brevity, only the results for TiTaHfNbZr HEA are provided.

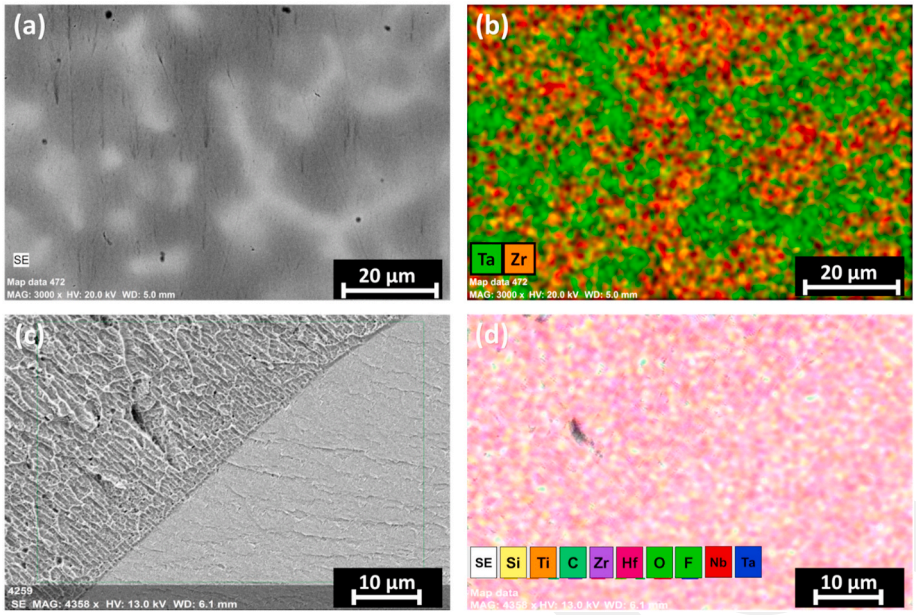

Fig. 12. BSE images and EDX results showing **(a)** non-homogeneous microstructure of the as-received TiTaHfMoZr, and **(b)** the corresponding elemental mapping where the green regions represent Ta-rich areas and red regions represent Zr-rich areas; **(c)** the fracture surface of TiTaHfNbZr following the CVN test, and **(d)** the corresponding elemental mapping. (For interpretation of the references to colour in this figure legend, the reader is referred to the Web version of this article.)

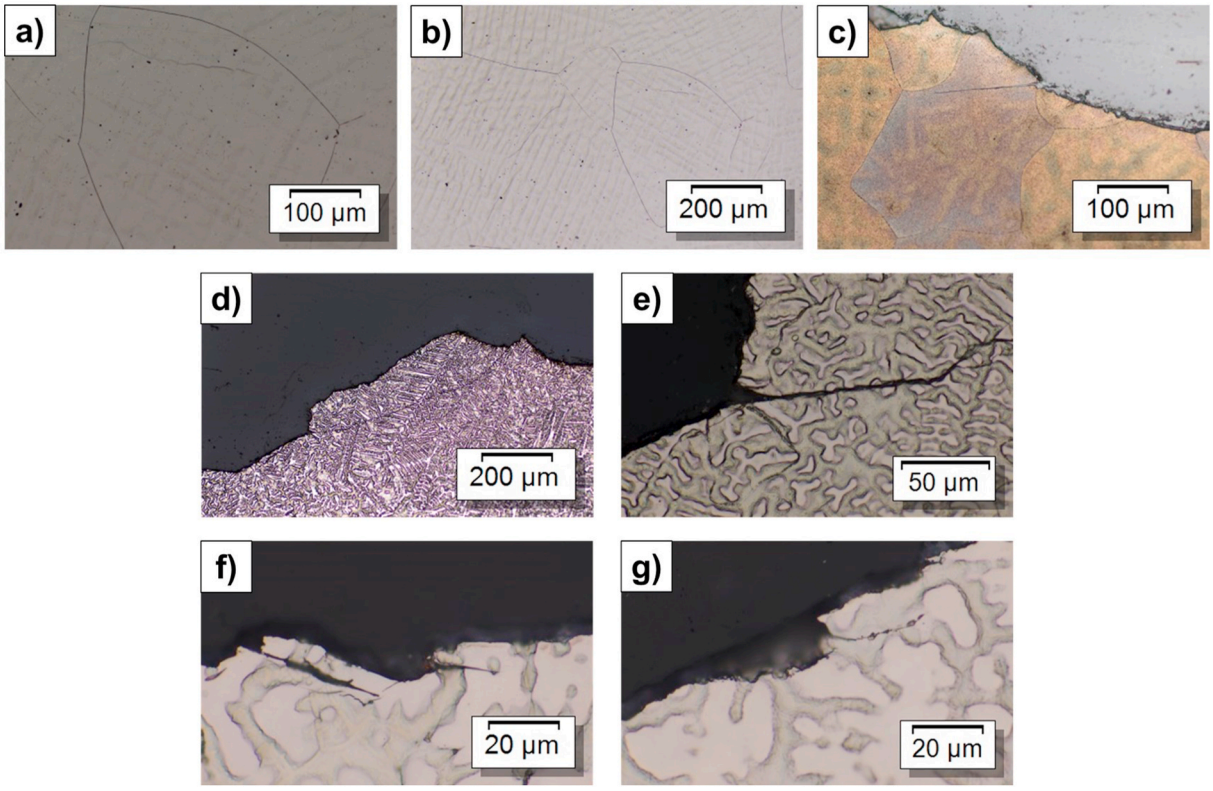

Fig. 13. Bright-field microscopy images showing **(a)** and **(b)**: the fracture surface of TiTaHfNb with cracking along grain boundaries, **(c)**: the fracture surface of TiTaHfNbZr with intergranular cracking and dendrites, and **(d)**, **(e)**, **(f)** and **(g)**: the fracture surface of TiTaHfMoZr with dendrites.

Visualization, Writing - original draft. **M.B. Yagci:** Formal analysis, Investigation, Methodology, Validation, Visualization, Writing - original draft. **D. Canadinc:** Conceptualization, Funding acquisition, Methodology, Project administration, Resources, Supervision, Writing - original draft. **G. Gerstein:** Formal analysis, Investigation, Methodology, Validation, Visualization, Writing - original draft. **B. Bal:** Formal analysis, Funding acquisition, Resources, Writing - original draft. **H.J. Maier:** Funding acquisition, Methodology, Project administration, Resources, Supervision, Writing - original draft.

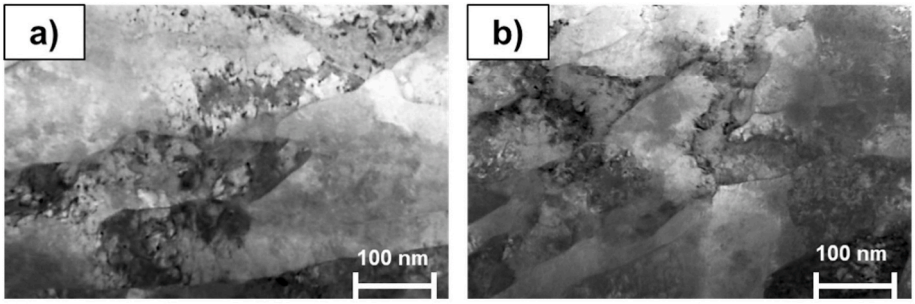

Fig. 14. TEM images showing the microstructure near fracture surfaces after CVN test: **(a)** TiTaHfNb, **(b)** TiTaHfNbZr.

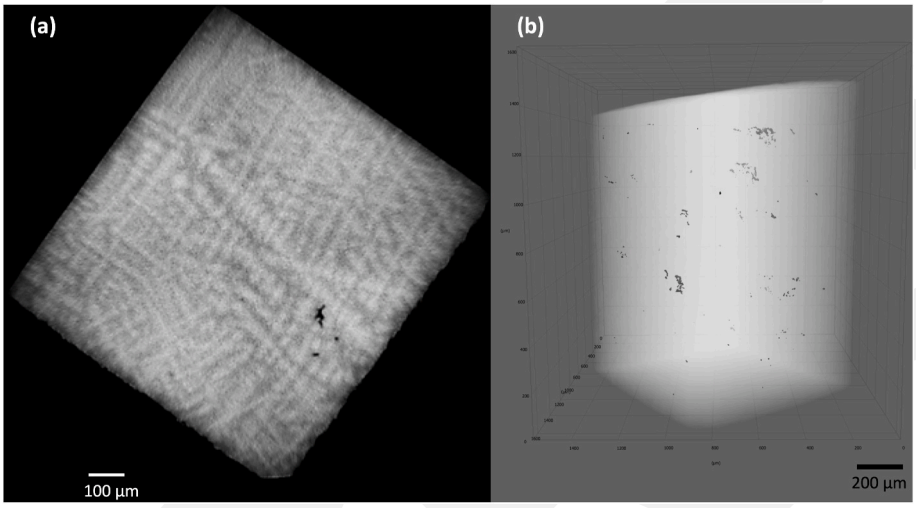

Fig. 15. XRM analysis showing **(a)** the presence of interdendritic pores and **(b)** their relatively small volume fraction within the bulk TiTaHfNbZr HEA.

Declaration of competing interest

The authors declare that they have no known competing financial interests or personal relationships that could have appeared to influence the work reported in this paper.

Acknowledgments

This study was supported by the BAGEP Award of the Science Academy. B. Bal acknowledges the AGU-BAP [grant number FAB-2017-77]. Financial support by the German Research Foundation (DFG, grant MA 1175/79-1 and grant 316923185) is also gratefully acknowledged. The authors also thank Mr. Mehmet Fazil Kapci for his help with the compression experiments.

References

[1] M. Niinomi, Mechanical properties of biomedical titanium alloys, Mater. Sci. Eng.A 243 (1998) 231–236, https://doi.org/10.1016/S0921-5093(97)00806-X.
[2] M. Niinomi, Recent metallic materials for biomedical applications, Metall. Mater. Trans. 33 (2002) 477–486, https://doi.org/10.1007/s11661-002-0109-2.
[3] M.P. Staiger, A.M. Pietak, J. Huadmai, G. Dias, Magnesium and its alloys as orthopedic biomaterials: a review, Biomaterials 27 (2006) 1728–1734, https://doi.org/10.1016/j.biomaterials.2005.10.003.
[4] Q. Chen, G.A. Thouas, Metallic implant biomaterials, Mater. Sci. Eng. R Rep. 87 (2015) 1–57, https://doi.org/10.1016/j.mser.2014.10.001.
[5] R. Van Noort, Titanium: the implant material of today, J. Mater. Sci. 22 (1987) 3801–3811, https://doi.org/10.1007/BF01133326.
[6] T. Akahori, M. Niinomi, Fracture characteristics of fatigued Ti–6Al–4V ELI as an implant material, Mater. Sci. Eng.A 243 (1998) 237–243, https://doi.org/10.1016/S0921-5093(97)00807-1.
[7] S. Sanivarapu, S. Moogla, R. Kuntcham, L. Kolaparthy, Implant fractures: rare but not exceptional, J. Indian Soc. Periodontol. 20 (2016) 6, https://doi.org/10.4103/0972-124X.154190.
[8] C.N. Elias, J.H.C. Lima, R. Valiev, M.A. Meyers, Biomedical applications of titanium and its alloys, JOM 60 (2008) 46–49, https://doi.org/10.1007/s11837-008-0031-1.
[9] Y. Li, C. Yang, H. Zhao, S. Qu, X. Li, Y. Li, New developments of Ti-based alloys for biomedical applications, Materials (Basel) 7 (2014) 1709–1800, https://doi.org/10.3390/ma7031709.
[10] M.F. López, J.A. Jiménez, A. Gutiérrez, Corrosion study of surface-modified vanadium-free titanium alloys, Electrochim. Acta (2003), https://doi.org/10.1016/S0013-4686(03)00006-9.
[11] M. Niinomi, M. Nakai, J. Hieda, Development of new metallic alloys for biomedical applications, Acta Biomater. 8 (2012) 3888–3903, https://doi.org/10.1016/j.actbio.2012.06.037.
[12] Y. Yuan, Y. Wu, Z. Yang, X. Liang, Z. Lei, H. Huang, H. Wang, X. Liu, K. An, W. Wu, Z. Lu, Formation, structure and properties of biocompatible TiZrHfNbTa high-entropy alloys, Mater. Res. Lett. 7 (2019) 225–231, https://doi.org/10.1080/21663831.2019.1584592.
[13] C. Oldani, A. Dominguez, Titanium as a biomaterial for implants, in: Recent Adv. Arthroplast., InTech, 2012, https://doi.org/10.5772/27413.
[14] S. Rajendran, J. Paulraj, P. Rengan, J. Jeyasundari, M. Manivannan, Corrosion behaviour of metals in artificial saliva in presence of spirulina powder, J. Dent. 1 (2009) 1–8.
[15] S. Rao, T. Ushida, T. Tateishi, Y. Okazaki, S. Asao, Effect of Ti, Al, and V ions on the relative growth rate of fibroblasts (L929) and osteoblasts (MC3T3-E1) cells, Bio Med. Mater. Eng. 6 (1996) 79–86. http://www.ncbi.nlm.nih.gov/pubmed/8761518.
[16] S.G. Steinemann, Metal implants and surface reactions, Injury 27 (1996), https://doi.org/10.1016/0020-1383(96)89027-9. S/C16-S/C22.
[17] L.N. Miotto, L.M.G. Fais, A.L.R. Ribeiro, L.G. Vaz, Surface properties of Ti-35Nb-7Zr-5Ta, J. Prosthet. Dent 116 (2016) 102–111, https://doi.org/10.1016/j.prosdent.2015.10.024.
[18] E. Kobayashi, T.J. Wang, H. Doi, T. Yoneyama, H. Hamanaka, Mechanical properties and corrosion resistance of Ti-6Al-7Nb alloy dental castings, J. Mater. Sci. Mater. Med. 9 (1998) 567–574, https://doi.org/10.1023/A:1008909408948.
[19] S. Tamilselvi, V. Raman, N. Rajendran, Corrosion behaviour of Ti–6Al–7Nb and Ti–6Al–4V ELI alloys in the simulated body fluid solution by electrochemical impedance spectroscopy, Electrochim. Acta 52 (2006) 839–846, https://doi.org/10.1016/j.electacta.2006.06.018.
[20] M.A. Khan, R.L. Williams, D.F. Williams, He corrosion behaviour of Ti-6Al-4V, Ti-6Al-7Nb and Ti-13Nb-13Zr in protein solutions. T, Biomaterials, 1999, https://doi.org/10.1016/S0142-9612(98)00217-8.

[21] Y. Okazaki, S. Rao, Y. Ito, T. Tateishi, Corrosion resistance, mechanical properties, corrosion fatigue strength and cytocompatibility of new Ti alloys without Al and V, Biomaterials 19 (1998) 1197–1215, https://doi.org/10.1016/S0142-9612(97)00235-4.

[22] Y. Okazaki, T. Tateishi, Y. Ito, Corrosion resistance of implant alloys in pseudo physiological solution and role of alloying elements in passive films, Mater. Trans. JIM. 38 (1997) 78–84, https://doi.org/10.2320/matertrans1989.38.78.

[23] M. Niinomi, Metallic biomaterials, J. Artif. Organs 11 (2008) 105–110, https://doi.org/10.1007/s10047-008-0422-7.

[24] D. Kuroda, H. Kawasaki, A. Yamamoto, S. Hiromoto, T. Hanawa, Mechanical properties and microstructures of new Ti-Fe-Ta and Ti-Fe-Ta-Zr system alloys, in: Mater. Sci. Eng. C, 2005, https://doi.org/10.1016/j.msec.2005.04.004.

[25] D. Raducanu, V.D. Cojocaru, A. Nocivin, I. Cinca, N. Serban, E.M. Cojocaru, Contributions to mechanical characteristics improvement of some biomedical TNTZ alloys by adding Fe, Si, and O: a comparative study, JOM 71 (2019) 264–271, https://doi.org/10.1007/s11837-018-3091-x.

[26] M. Todai, T. Nagase, T. Hori, A. Matsugaki, A. Sekita, T. Nakano, Novel TiNbTaZrMo high-entropy alloys for metallic biomaterials, Scripta Mater. 129 (2017) 65–68, https://doi.org/10.1016/j.scriptamat.2016.10.028.

[27] M.T. Mohammed, Z.A. Khan, A.N. Siddiquee, Beta titanium alloys: the lowest elastic modulus for biomedical applications: a review surface modifications through FSP view project machining view project, Int. J. Chem. Nucl. Metall. Mater. Eng. 8 (2014) 726–731. https://www.researchgate.net/publication/265396160.

[28] C.W. Gealh, V. Mazzo, F. Barbi, E.T. Camarini, Osseointegrated implant fracture: causes and treatment, J. Oral Implantol. (2011), https://doi.org/10.1563/AAID-JOI-D-09-00135.1.

[29] N. Tagger Green, E.E. Machtei, J. Horwitz, M. Peled, Fracture of dental implants: literature review and report of a case, Implant Dent. 11 (2002) 137–143, https://doi.org/10.1097/00008505-200204000-00014.

[30] K. Shemtov-Yona, D. Rittel, On the mechanical integrity of retrieved dental implants, J. Mech. Behav. Biomed. Mater. (2015), https://doi.org/10.1016/j.jmbbm.2015.05.014.

[31] A. Piattelli, A. Scarano, M. Piattelli, E. Vaia, S. Matarasso, Hollow implants retrieved for fracture: a light and scanning electron microscope analysis of 4 cases, J. Periodontol. 69 (1998) 185–189, https://doi.org/10.1902/jop.1998.69.2.185.

[32] A. Piattelli, M. Piattelli, A. Scarano, L. Montesani, Light and scanning electron microscopic report of four fractured implants, Int. J. Oral Maxillofac. Implants 13 (1998) 561–564.

[33] A.A. Siddiqui, R. Caudill, Proceedings of the fourth international symposium on implant dentistry: focus on esthetics, J. Prosthet. Dent (1994), https://doi.org/10.1016/0022-3913(94)90295-x.

[34] Y. Zhang, T.T. Zuo, Z. Tang, M.C. Gao, K.A. Dahmen, P.K. Liaw, Z.P. Lu, Microstructures and properties of high-entropy alloys, Prog. Mater. Sci. 61 (2014) 1–93, https://doi.org/10.1016/j.pmatsci.2013.10.001.

[35] D.B. Miracle, O.N. Senkov, A critical review of high entropy alloys and related concepts, Acta Mater. 122 (2017) 448–511, https://doi.org/10.1016/j.actamat.2016.08.081.

[36] Y. Zhang, X. Yang, P.K. Liaw, Alloy design and properties optimization of high-entropy alloys, JOM 64 (2012) 830–838, https://doi.org/10.1007/s11837-012-0366-5.

[37] L. Vinet, A. Zhedanov, A 'missing' family of classical orthogonal polynomials, J. Phys. A Math. Theor. 44 (2011), 085201, https://doi.org/10.1088/1751-8113/44/8/085201.

[38] Y. Qiu, S. Thomas, M.A. Gibson, H.L. Fraser, N. Birbilis, Corrosion of high entropy alloys, Npj Mater. Degrad. 1 (2017) 15, https://doi.org/10.1038/s41529-017-0009-y.

[39] X.W. Qiu, Y.P. Zhang, L. He, C.G. Liu, Microstructure and corrosion resistance of AlCrFeCuCo high entropy alloy, J. Alloys Compd. 549 (2013) 195–199, https://doi.org/10.1016/j.jallcom.2012.09.091.

[40] C. Li, J.C. Li, M. Zhao, Q. Jiang, Effect of aluminum contents on microstructure and properties of AlxCoCrFeNi alloys, J. Alloys Compd. 504 (2010), https://doi.org/10.1016/j.jallcom.2010.03.111. S515–S518.

[41] Z.D. Han, H.W. Luan, X. Liu, N. Chen, X.Y. Li, Y. Shao, K.F. Yao, Microstructures and mechanical properties of Ti NbMoTaW refractory high-entropy alloys, Mater. Sci. Eng.A 712 (2018) 380–385, https://doi.org/10.1016/j.msea.2017.12.004.

[42] T.-T. Shun, L.-Y. Chang, M.-H. Shiu, Microstructures and mechanical properties of multiprincipal component CoCrFeNiTix alloys, Mater. Sci. Eng.A 556 (2012) 170–174, https://doi.org/10.1016/j.msea.2012.06.075.

[43] O.N. Senkov, J.M. Scott, S.V. Senkova, D.B. Miracle, C.F. Woodward, Microstructure and room temperature properties of a high-entropy TaNbHfZrTi alloy, J. Alloys Compd. 509 (2011) 6043–6048, https://doi.org/10.1016/j.jallcom.2011.02.171.

[44] X.F. Wang, Y. Zhang, Y. Qiao, G.L. Chen, Novel microstructure and properties of multicomponent CoCrCuFeNiTix alloys, Intermetallics 15 (2007) 357–362, https://doi.org/10.1016/j.intermet.2006.08.005.

[45] O.N. Senkov, G.B. Wilks, D.B. Miracle, C.P. Chuang, P.K. Liaw, Refractory high-entropy alloys, Intermetallics 18 (2010) 1758–1765, https://doi.org/10.1016/j.intermet.2010.05.014.

[46] Y. Qiu, M.A. Gibson, H.L. Fraser, N. Birbilis, Corrosion characteristics of high entropy alloys, Mater. Sci. Technol. 31 (2015) 1235–1243, https://doi.org/10.1179/1743284715Y.0000000026.

[47] Z. Tang, L. Huang, W. He, P. Liaw, Alloying and processing effects on the aqueous corrosion behavior of high-entropy alloys, Entropy 16 (2014) 895–911, https://doi.org/10.3390/e16020895.

[48] Y.-J. Hsu, W.-C. Chiang, J.-K. Wu, Corrosion behavior of FeCoNiCrCux high-entropy alloys in 3.5% sodium chloride solution, Mater. Chem. Phys. 92 (2005) 112–117, https://doi.org/10.1016/j.matchemphys.2005.01.001.

[49] B. Gludovatz, A. Hohenwarter, D. Catoor, E.H. Chang, E.P. George, R.O. Ritchie, ChemInform abstract: a fracture-resistant high-entropy alloy for cryogenic applications, ChemInform 45 (2014), https://doi.org/10.1002/chin.201447007.

[50] Z. Zhang, M.M. Mao, J. Wang, B. Gludovatz, Z. Zhang, S.X. Mao, E.P. George, Q. Yu, R.O. Ritchie, Nanoscale origins of the damage tolerance of the high-entropy alloy CrMnFeCoNi, Nat. Commun. 6 (2015) 10143, https://doi.org/10.1038/ncomms10143.

[51] R. Sriharitha, B.S. Murty, R.S. Kottada, Alloying, thermal stability and strengthening in spark plasma sintered AlxCoCrCuFeNi high entropy alloys, J. Alloys Compd. 583 (2014) 419–426, https://doi.org/10.1016/j.jallcom.2013.08.176.

[52] W. Zhang, P.K. Liaw, Y. Zhang, Science and technology in high-entropy alloys, Sci. China Mater. 61 (2018) 2–22, https://doi.org/10.1007/s40843-017-9195-8.

[53] G. Popescu, B. Ghiban, C.A. Popescu, L. Rosu, R. Truscă, I. Carcea, V. Soare, D. Dumitrescu, I. Constantin, M.T. Olaru, B.A. Carlan, New TiZrNbTaFe high entropy alloy used for medical applications, IOP Conf. Ser. Mater. Sci. Eng. 400 (2018), 022049, https://doi.org/10.1088/1757-899X/400/2/022049.

[54] V. Braic, M. Balaceanu, M. Braic, A. Vladescu, S. Panseri, A. Russo, Characterization of multi-principal-element (TiZrNbHfTa)N and (TiZrNbHfTa)C coatings for biomedical applications, J. Mech. Behav. Biomed. Mater. 10 (2012) 197–205, https://doi.org/10.1016/j.jmbbm.2012.02.020.

[55] B. Ghiban, G. Popescu, C. Lazar, L. Rosu, I. Constantin, M. Olaru, B. Carlan, Corrosion behaviour in human stimulation media of a high entropy titan-based alloy, IOP Conf. Ser. Mater. Sci. Eng. 374 (2018), 012004, https://doi.org/10.1088/1757-899X/374/1/012004.

[56] C.B. Aksoy, D. Canadinc, M.B. Yagci, Assessment of Ni ion release from TiTaHfNbZr high entropy alloy coated NiTi shape memory substrates in artificial saliva and gastric fluid, Mater. Chem. Phys. 236 (2019) 121802, https://doi.org/10.1016/j.matchemphys.2019.121802.

[57] X. Qiu, Corrosion behavior of Al2CrFeCo CuNiTi high-entropy alloy coating in alkaline solution and salt solution, Results Phys 12 (2019) 1737–1741, https://doi.org/10.1016/j.rinp.2019.01.090.

[58] Y. Shi, B. Yang, P. Liaw, Corrosion-resistant high-entropy alloys, A Review, Metals (Basel) 7 (2017) 43, https://doi.org/10.3390/met7020043.

[59] S. Gurel, M.B. Yagci, B. Bal, D. Canadinc, Corrosion behavior of novel Titanium-based high entropy alloys designed for medical implants, Mater. Chem. Phys. 254 (2020) 123377, https://doi.org/10.1016/j.matchemphys.2020.123377.

[60] C.-C. Juan, M.-H. Tsai, C.-W. Tsai, C.-M. Lin, W.-R. Wang, C.-C. Yang, S.-K. Chen, S.-J. Lin, J.-W. Yeh, Enhanced mechanical properties of HfMoTaTiZr and HfMoNbTaTiZr refractory high-entropy alloys, Intermetallics 62 (2015) 76–83, https://doi.org/10.1016/j.intermet.2015.03.013.

[61] S.-P. Wang, J. Xu, TiZrNbTaMo high-entropy alloy designed for orthopedic implants: as-cast microstructure and mechanical properties, Mater. Sci. Eng. C 73 (2017) 80–89, https://doi.org/10.1016/j.msec.2016.12.057.

[62] K.-K. Tseng, C.-C. Juan, S. Tso, H.-C. Chen, C.-W. Tsai, J.-W. Yeh, Effects of Mo, Nb, Ta, Ti, and Zr on mechanical properties of equiatomic Hf-Mo-Nb-Ta-Ti-Zr alloys, Entropy 21 (2018) 15, https://doi.org/10.3390/e21010015.

[63] T. Nagase, M. Todai, T. Hori, T. Nakano, Microstructure of equiatomic and non-equiatomic Ti-Nb-Ta-Zr-Mo high-entropy alloys for metallic biomaterials, J. Alloys Compd. 753 (2018) 412–421, https://doi.org/10.1016/j.jallcom.2018.04.082.

[64] O.N. Senkov, G.B. Wilks, J.M. Scott, D.B. Miracle, Mechanical properties of Nb25Mo25Ta25W25 and V20Nb20Mo20Ta20W20 refractory high entropy alloys, Intermetallics 19 (2011) 698–706, https://doi.org/10.1016/j.intermet.2011.01.004.

[65] Y.D. Wu, Y.H. Cai, T. Wang, J.J. Si, J. Zhu, Y.D. Wang, X.D. Hui, A refractory Hf25Nb25Ti25Zr25 high-entropy alloy with excellent structural stability and tensile properties, Mater. Lett. 130 (2014) 277–280, https://doi.org/10.1016/j.matlet.2014.05.134.

[66] G. Dirras, L. Lilensten, P. Djemia, M. Laurent-Brocq, D. Tingaud, J.-P. Couzinié, L. Perrière, T. Chauveau, I. Guillot, Elastic and plastic properties of as-cast equimolar TiHfZrTaNb high-entropy alloy, Mater. Sci. Eng.A 654 (2016) 30–38, https://doi.org/10.1016/j.msea.2015.12.017.

[67] O.N. Senkov, S.L. Semiatin, Microstructure and properties of a refractory high-entropy alloy after cold working, J. Alloys Compd. 649 (2015) 1110–1123, https://doi.org/10.1016/j.jallcom.2015.07.209.

[68] H. Huang, Y. Wu, J. He, H. Wang, X. Liu, K. An, W. Wu, Z. Lu, Phase-transformation ductilization of brittle high-entropy alloys via metastability engineering, Adv. Mater. (2017), https://doi.org/10.1002/adma.201701678.

[69] J. Zýka, J. Málek, J. Veselý, F. Lukáč, J. Čížek, J. Kuriplach, O. Melikhova, Microstructure and room temperature mechanical properties of different 3 and 4 element medium entropy alloys from HfNbTaTiZr system, Entropy 21 (2019) 114, https://doi.org/10.3390/e21020114.

[70] A. Motallebzadeh, M.B. Yagci, E. Bedir, C.B. Aksoy, D. Canadinc, Mechanical properties of TiTaHfNbZr high-entropy alloy coatings deposited on NiTi shape memory alloy substrates, Metall. Mater. Trans. 49 (2018), https://doi.org/10.1007/s11661-018-4605-4, 1992–1997.

[71] C.C. Juan, M.H. Tsai, C.W. Tsai, C.M. Lin, W.R. Wang, C.C. Yang, S.K. Chen, S. J. Lin, J.W. Yeh, Enhanced mechanical properties of HfMoTaTiZr and HfMoNbTaTiZr refractory high-entropy alloys, Intermetallics 62 (2015) 76–83, https://doi.org/10.1016/j.intermet.2015.03.013.

[72] Astm E 23-12c, Standard test methods for notched bar impact testing of metallic materials, Standards i (2013) 1–25, https://doi.org/10.1520/E0023-12C.2.

[73] S.-P. Wang, J. Xu, (TiZrNbTa)-Mo high-entropy alloys: dependence of microstructure and mechanical properties on Mo concentration and modeling of solid solution strengthening, Intermetallics 95 (2018) 59–72, https://doi.org/10.1016/j.intermet.2018.01.017.
[74] A. Motallebzadeh, N.S. Peighambardoust, S. Sheikh, H. Murakami, S. Guo, D. Canadinc, Microstructural, mechanical and electrochemical characterization of TiZrTaHfNb and Ti1.5ZrTa0.5Hf0.5Nb0.5 refractory high-entropy alloys for biomedical applications, Intermetallics 113 (2019) 106572, https://doi.org/10.1016/j.intermet.2019.106572.
[75] J.-P. Couzinié, G. Dirras, Body-centered cubic high-entropy alloys: from processing to underlying deformation mechanisms, Mater. Char. 147 (2019) 533–544, https://doi.org/10.1016/j.matchar.2018.07.015.
[76] F. Lukáč, M. Dudr, J. Čížek, P. Harcuba, T. Vlasák, M. Janeček, J. Kuriplach, J. Moon, H.S. Kim, J. Zýka, J. Málek, Defects in high entropy alloy HfNbTaTiZr prepared by high pressure torsion, Acta Phys. Pol., A 134 (2018) 891–894, https://doi.org/10.12693/APhysPolA.134.891.
[77] A. Andrieu, A. Pineau, P. Joly, F. Roch, On modeling of thermal embrittlement in pwr steels using the local approach to fracture, 13th Int. Conf. Fract. 2013 7 (2013) 5526–5535. ICF 2013.
[78] R.W. Hertzberg, R.P. Vinci, J.L. Hertzberg, Deformation and fracture mechanics of engineering materials, Wiley, 2020. https://books.google.com.tr/books?id=43ntDwAAQBAJ.
[79] F. Khan, S.K. Panigrahi, Age hardening, fracture behavior and mechanical properties of QE22 Mg alloy, J. Magnes. Alloy. 3 (2015) 210–217, https://doi.org/10.1016/j.jma.2015.08.002.
[80] I. Kopova, J. Stráský, P. Harcuba, M. Landa, M. Janeček, L. Bačákova, Newly developed Ti–Nb–Zr–Ta–Si–Fe biomedical beta titanium alloys with increased strength and enhanced biocompatibility, Mater. Sci. Eng. C 60 (2016) 230–238, https://doi.org/10.1016/j.msec.2015.11.043.
[81] C.C. Juan, K.K. Tseng, W.L. Hsu, M.H. Tsai, C.W. Tsai, C.M. Lin, S.K. Chen, S.J. Lin, J.W. Yeh, Solution strengthening of ductile refractory HfMoxNbTaTiZr high-entropy alloys, Mater. Lett. 175 (2016) 284–287, https://doi.org/10.1016/j.matlet.2016.03.133.
[82] K.-T. Park, S.T. Yang, J.C. Earthman, F.A. Mohamed, The effect of impurities on ductility and cavitation in superplastic Zn-22%Al alloy, Mater. Sci. Eng., A 188 (1994) 59–67, https://doi.org/10.1016/0921-5093(94)90356-5.
[83] V. Kochubey, H. Al-Badairy, G. Tatlock, J. Le-Coze, D. Naumenko, W. J. Quadakkers, Effects of minor additions and impuruties onoxidation behaviour of FeCrAl alloys. Development of novel surface coatings compositions, Mater. Corros. 56 (2005) 848–853, https://doi.org/10.1002/maco.200503915.
[84] A. Ayyagari, R. Salloom, S. Muskeri, S. Mukherjee, Low activation high entropy alloys for next generation nuclear applications, Materialia 4 (2018) 99–103, https://doi.org/10.1016/j.mtla.2018.09.014.
[85] A. Ayyagari, V. Hasannaeimi, H. Arora, S. Mukherjee, Electrochemical and friction characteristics of metallic glass composites at the microstructural length-scales, Sci. Rep. 8 (2018) 906, https://doi.org/10.1038/s41598-018-19488-7.